INTERNATIONAL JOURNAL FOR NUMERICAL METHODS IN FLUIDS, VOL. 14, 197–215 (1992)

SURFACE TENSION AND BUOYANCY-DRIVEN FLOW IN A NON-ISOTHERMAL LIQUID BRIDGE

YIQIANG ZHANG AND J. IWAN D. ALEXANDER

Center for Microgravity and Materials Research, University of Alabama in Huntsville, Huntsville, AL 35899, U.S.A.

SUMMARY

The Navier–Stokes–Boussinesq equations governing the transport of momentum, mass and heat in a non-isothermal liquid bridge with a temperature-dependent surface tension are solved using a vorticity–stream-function formulation together with a non-orthogonal co-ordinate transformation. The equations are discretized using a pseudo-unsteady semi-implicit finite difference scheme and are solved by the ADI method. A Picard-type iteration is adopted which consists of inner and outer iterative processes. The outer iteration is used to update the shape of the free surface. Two schemes have been used for the outer iteration; both use the force balance normal to the free surface as the distinguished boundary condition. The first scheme involves successive approximation by the direct solution of the distinguished boundary condition. The second scheme uses the artificial force imbalance between the fluid pressure, viscous and capillary forces at the free surface which arises when the boundary condition for force balance normal to the surface is not satisfied. This artificial imbalance is then used to change the surface shape until the distinguished boundary condition is satisfied. These schemes have been used to examine a variety of model liquid bridge situations including purely thermocapillary-driven flow situations and mixed thermocapillary- and bouyancy-driven flow.

KEY WORDS Thermocapillary flow Buoyancy Free surface Finite difference Picard iteration ADI

1. INTRODUCTION

The computation of solutions to the steady free boundary problem of mixed thermocapillary- and buoyancy-driven convection in a non-isothermal cylindrical liquid bridge is complicated by the strongly non-linear boundary conditions at the unknown free surface. Most studies to date have avoided the computation of the free surface shape and assumed that the liquid surface is a circular cylinder[1–6] or have imposed a non-circular cylindrical surface shape.[7] These models have involved either half-zone configurations (where the liquid bridge is held between rigid disks of different temperature) or full zones (where the liquid bridge is held between two solids of equal temperature). The full zone models are motivated by the floating zone crystal growth process.[8] Recently, Duranceau and Brown[9] have approached the full zone crystal growth problem using the finite element method and have computed the shape of the liquid surface as well as the melt–crystal and melt–feed rod surfaces together with interacting thermocapillary and buoyant convective flow. Lan and Kou[10] have also approached the full zone problem using a finite volume method but restricted their calculations to the zero-gravity case for which the surface deformation from the circular cylindrical shape is minimal and buoyancy-driven flow is absent. Hyer *et al.*[11] have used a finite element method, which is well suited to irregular geometries, to compute

0271–2091/92/020197–19$09.50

Received October 1990
Revised April 1991

interacting thermocapillary and buoyant convective flow in full and half-zone configurations but did not consider solidification.

Recently, finite difference methods have been used to solve problems with free and moving boundary geometries using various mapping techniques.[12] These methods are also applicable to the free boundary problem associated with liquid bridges and floating zones. Kang and Leal[13] used the finite difference method with orthogonal boundary-fitted co-ordinates to study the deformation of a bubble. The boundary-fitted mapping scheme requires the solution of a coupled set of Laplace equations to determine the new grid to be generated at each outer iteration.

In the present investigation the governing equations are recast in terms of a vorticity–stream-function formulation together with a non-orthogonal co-ordinate transformation. The latter allows an irregular free boundary to coincide with a co-ordinate line (or surface) without the need to solve a coupled set of Laplace equations. The resulting equations are discretized using a pseudo-unsteady semi-implicit difference scheme and solved by the ADI method. The combination of the above methods provides a reasonably accurate and economical solution procedure. Four boundary conditions are specified at the free surface: the kinematic boundary condition, the balance of energy across the surface and the balance of force normal and tangent to the surface. The energy balance, tangential force balance and kinematic conditions at the free surface are solved together with the Navier–Stokes and continuity equations, while the normal force balance condition is distinguished[14] to determine the free surface shape. In addition, an 'outer' iterative procedure is needed to locate the free surface. In this paper two outer iterative schemes are reported. The first scheme involves successive approximation by the direct solution of the force balance normal to the free surface. The second scheme, after Ryskin and Leal,[15] uses the force imbalance between the fluid pressure, viscous and capillary forces at the free surface which arises when the boundary condition for force balance normal to the surface is not satisfied. This artificial imbalance is used to drive the surface shape towards its equilibrium position (i.e. until the force balance condition is satisfied). These schemes are used to examine a variety of model liquid bridge situations including purely thermocapillary-driven flow situations and mixed buoyancy–thermocapillary-driven flow.

2. FORMULATION OF THE PROBLEM

2.1. Governing equations

Consider a cylindrical liquid bridge (see Figure 1) held between two parallel coaxial circular rigid disks of radius R_0 separated by a distance L. The liquid is a non-isothermal incompressible Newtonian fluid. The bridge is held between the disks by surface tension. The free surface of the bridge is a gas–liquid surface and the steady surface shape is described by $r = R(z)$. Each disk is maintained at a constant temperature T_0. Surface heating is provided through an ambient temperature $T_\infty(z)$. Radiative and convective heat transfer at the free surface are accounted for by a heat transfer coefficient h. In addition, we assume that the gravitational acceleration is parallel to the cylinder axis and that the velocity, temperature field and the deformation of the free surface are axisymmetric. Furthermore, we let the surface tension at the free surface vary linearly with temperature and assume that the Boussinesq approximation holds.

The governing equations are made dimensionless by scaling length, time and velocity with R_0, R_0/U^* and U^* respectively. Here U^* is a characteristic velocity given by

$$U^* = \frac{|\gamma|\Delta T}{\mu},$$

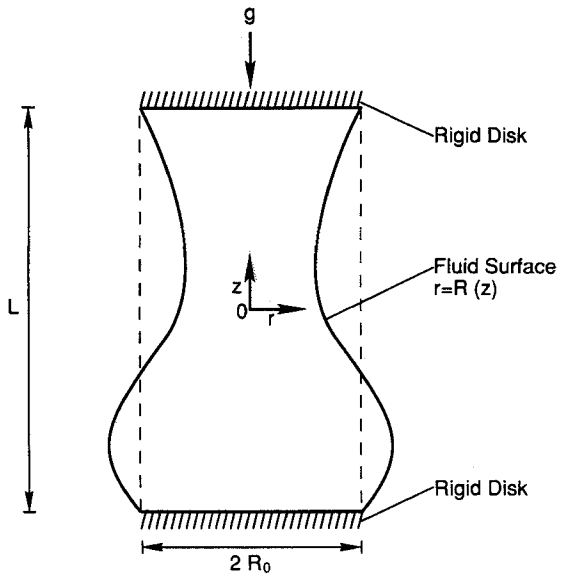

Figure 1. Liquid bridge model

where $\Delta T = T_{max} - T_{min}$ represents the maximum temperature difference at the surface, $|\gamma|$ is the absolute value of the derivative of the surface tension with respect to temperature and μ is the dynamic viscosity.

We shall refer to a 'half-zone' model when the end disks are held at the maximum and minimum temperatures respectively and a 'full zone' when the temperature maximum occurs between the disks. For a full zone we shall take the ambient temperature $T_\infty(z)$ to be parabolic and take T_{max} to be $T_\infty(0)$ and T_{min} to be $T(\pm\Lambda/2)$, where $\Lambda = L/R_0$ is the aspect ratio.

The non-dimensional pressure is

$$p = \frac{p^* + \rho_0 g z}{\rho_0 U^{*2}} R_0,$$

where p^* is the dimensional pressure, g is the gravitational acceleration, z is the dimensionless axial co-ordinate and ρ_0 is the density corresponding to the reference temperature. The temperature is rendered dimensionless using $T_{max} - T_{min}$. With these scales the dimensionless steady state equations in a cylindrical co-ordinate system can be written as

$$\frac{1}{r}\frac{\partial(ru)}{\partial r} + \frac{\partial w}{\partial z} = 0, \tag{1}$$

$$u\frac{\partial u}{\partial r} + w\frac{\partial u}{\partial z} = -\frac{\partial p}{\partial r} + \frac{1}{Re}\left(\frac{\partial^2 u}{\partial r^2} + \frac{1}{r}\frac{\partial u}{\partial r} + \frac{\partial^2 u}{\partial z^2} - \frac{u}{r^2}\right), \tag{2}$$

$$u\frac{\partial u}{\partial r} + w\frac{\partial w}{\partial z} = -\frac{\partial p}{\partial z} + \frac{1}{Re}\left(\frac{\partial^2 w}{\partial r^2} + \frac{1}{r}\frac{\partial w}{\partial r} + \frac{\partial^2 w}{\partial z^2}\right) + \frac{Gr}{Re^2}T, \tag{3}$$

$$u\frac{\partial T}{\partial r} + w\frac{\partial T}{\partial z} = \frac{1}{Ma}\left(\frac{\partial^2 T}{\partial r^2} + \frac{1}{r}\frac{\partial T}{\partial r} + \frac{\partial^2 T}{\partial z^2}\right), \tag{4}$$

where the Reynolds number Re, Marangoni number Ma and Grashof number Gr are respectively

$$Re=\frac{R_0 U^*}{\nu}, \qquad Ma=\frac{|\gamma|\Delta T R_0}{\mu\kappa}, \qquad Gr=\frac{g\beta\Delta T R_0^3}{\nu^2}.$$

Here ν is the kinematic viscosity, κ is the thermal diffusivity, β is the volumetric thermal expansion coefficient and g is the gravitational acceleration.

2.2. *Boundary conditions*

At the disks the boundary conditions are

$$u=w=T=0 \quad \text{at } z=\pm\Lambda/2, \tag{5}$$

and the symmetry conditions at the centreline $r=0$ are

$$u=\frac{\partial w}{\partial r}=\frac{\partial T}{\partial r}=0. \tag{6}$$

The boundary conditions at the free surface $r=R(z)$ take the form

$$p-Gz+\lambda=\frac{2Re^{-1}}{1+(\partial R/\partial z)^2}\left[\frac{\partial u}{\partial r}+\left(\frac{\partial R}{\partial z}\right)^2\frac{\partial w}{\partial z}-\frac{\partial R}{\partial z}\left(\frac{\partial w}{\partial r}+\frac{\partial u}{\partial z}\right)\right] + \frac{Re^{-1}(C_0^{-1}-T)}{[1+(\partial R/\partial z)^2]^{3/2}}\left(\frac{1+(\partial R/\partial z)^2}{R}-\frac{\partial^2 R}{\partial z^2}\right), \tag{7}$$

$$\left[1-\left(\frac{\partial R}{\partial z}\right)^2\right]\left(\frac{\partial u}{\partial z}+\frac{\partial w}{\partial r}\right)+2\frac{\partial R}{\partial z}\left(\frac{\partial u}{\partial r}-\frac{\partial w}{\partial z}\right)=-\left[1+\left(\frac{\partial R}{\partial z}\right)^2\right]^{1/2}\left(\frac{\partial T}{\partial z}+\frac{\partial R}{\partial z}\frac{\partial T}{\partial r}\right), \tag{8}$$

$$u+w\frac{\partial R}{\partial z}=0, \tag{9}$$

$$\frac{1}{(1+(\partial R/\partial z)^2)^{1/2}}\left(\frac{\partial T}{\partial r}-\frac{\partial R}{\partial z}\frac{\partial T}{\partial z}\right)+Bi(T-T_\infty)=0, \tag{10}$$

where

$$C_0=\frac{\gamma\Delta T}{\gamma_0}, \qquad Bi=\frac{hR_0}{\kappa}, \qquad G=\frac{gR_0}{U^{*2}}$$

are the capillary number, Biot number and dimensionless gravitational acceleration respectively and γ_0 is the mean surface tension. The force balances at the free surface in the normal and tangential directions are given by equations (7) and (8) respectively. Equation (9) is the kinematic boundary condition at the liquid–gas surface. The thermal boundary condition at the surface is given by equation (10) with the dimensionless heat transfer coefficient Bi. The constant λ on the left-hand side of (7) represents a dimensionless reference pressure difference[9] across the surface. In liquid bridge model systems with fixed rigid disks such as the one discussed here, λ is determined by the constant volume constraint

$$V_0=\int_{-\Lambda/2}^{\Lambda/2}\pi R^2(z)\,dz\equiv\text{constant}. \tag{11}$$

Finally, the condition that the contact lines between the liquid end disks are fixed is

$$R=1 \quad \text{at } z=\pm\Lambda/2. \tag{12}$$

3. NUMERICAL METHOD

For the case of a two-dimensional axisymmetric flow the governing equations can be simplified by introducing the streamfunction ψ and vorticity ω as new dependent variables:

$$u=\frac{1}{r}\frac{\partial\psi}{\partial z}, \qquad w=\frac{-1}{r}\frac{\partial\psi}{\partial r}, \tag{13}$$

$$\omega=\frac{\partial u}{\partial z}-\frac{\partial w}{\partial r}. \tag{14}$$

From (13), (14), (2) and (3) one obtains for ω

$$u\frac{\partial\omega}{\partial r}+w\frac{\partial\omega}{\partial z}-\frac{\omega u}{r}=\frac{1}{Re}\left(\frac{\partial^2\omega}{\partial r^2}+\frac{1}{r}\frac{\partial\omega}{\partial r}+\frac{\partial^2\omega}{\partial z^2}\right)-\frac{1}{Re}\frac{\omega}{r^2}-\frac{Gr}{Re^2}\frac{\partial T}{\partial r}. \tag{15}$$

Substitution of (13) into (14) yields

$$r\omega=\frac{\partial^2\psi}{\partial r^2}-\frac{1}{r}\frac{\partial\psi}{\partial r}+\frac{\partial^2\psi}{\partial z^2}. \tag{16}$$

The original set of three equations governing mass and momentum has thus been reduced to two equations governing the streamfunction and vorticity.

The steady free boundary problem for a cylindrical liquid bridge is solved iteratively, since the location of the free surface is *a priori* unknown. To obtain a solution, we adopt a Picard iterative procedure[12] as follows.

1. Guess the free surface shape for the initial iterate.
2. Obtain the approximate temperature and velocity fields by transforming the governing equations and boundary conditions to a circular cylindrical domain via a non-orthogonal transformation and solve them using a pseudo-unsteady semi-implicit method.
3. Obtain the pressure at the free surface by integrating the transformed momentum equation.
4. Use the normal force balance condition at the free surface to decide how to update the free surface location.
5. Return to step 2. Repeat until convergence is obtained by satisfing all equations and boundary conditions to a specified degree of accuracy.

The details of this numerical procedure are discussed below.

3.1. Non-orthogonal transformation

At each outer iteration the region occupied by the liquid bridge is transformed into a fixed rectangular computational region using a non-orthogonal co-ordinate transformation, i.e.

$$\eta=z, \qquad \xi=\frac{r}{R(z,\tau)}. \tag{17}$$

For each iteration time τ this transforms the domain

$$-\Lambda/2<z<\Lambda/2, \qquad 0<r<R(z,\tau)$$

onto the rectangle

$$-\Lambda/2<z<\Lambda/2, \qquad 0<\xi<1.$$

It then follows that

$$\frac{\partial}{\partial r}\rightarrow\frac{1}{R}\frac{\partial}{\partial\zeta}, \qquad \frac{\partial}{\partial z}\rightarrow\frac{\partial}{\partial\eta}-\frac{\zeta}{R}\frac{\partial R}{\partial\eta}\frac{\partial}{\partial\zeta}. \tag{18}$$

The advantage of this transformation is that the free boundary coincides exactly with a co-ordinate line in a computational grid and regeneration of mesh during the outer iteration is avoided. The transformed governing equations now take the form

$$\frac{1}{R^2\zeta}\left(\frac{\partial\psi}{\partial\eta}\frac{\partial\omega}{\partial\zeta}-\frac{\partial\psi}{\partial\zeta}\frac{\partial\omega}{\partial\eta}\right)-\frac{u\omega}{R\zeta}=\frac{1}{Re}\left(\frac{\partial^2\omega}{\partial\eta^2}+A\frac{\partial^2\omega}{\partial\zeta^2}+B\frac{\partial\omega}{\partial\zeta}+C\frac{\partial^2\omega}{\partial\eta\partial\zeta}\right)-\frac{1}{Re}\frac{\omega}{R^2\zeta^2}-\frac{G_r}{Re^2}\frac{1}{R}\frac{\partial T}{\partial\zeta}. \tag{19}$$

$$\frac{1}{R^2\zeta}\left(\frac{\partial\psi}{\partial\eta}\frac{\partial T}{\partial\zeta}-\frac{\partial\psi}{\partial\zeta}\frac{\partial T}{\partial\eta}\right)=\frac{1}{Ma}\left(\frac{\partial^2T}{\partial\eta^2}+A\frac{\partial^2T}{\partial\zeta^2}+B\frac{\partial T}{\partial\zeta}+C\frac{\partial^2T}{\partial\eta\partial\zeta}\right), \tag{20}$$

$$\frac{\partial^2\psi}{\partial\eta^2}+A\frac{\partial^2\psi}{\partial\zeta^2}+B^*\frac{\partial\psi}{\partial\zeta}+C\frac{\partial^2\psi}{\partial\eta\partial\zeta}=R\zeta\omega, \tag{21}$$

where

$$A=\left(\frac{\zeta}{R}\frac{\partial R}{\partial\eta}\right)^2+\frac{1}{R^2},$$

$$B=\left[2\left(\frac{1}{R}\frac{\partial R}{\partial\eta}\right)^2-\frac{1}{R}\frac{\partial^2R}{\partial\eta^2}\right]\zeta+\frac{1}{R^2\zeta},$$

$$B^*=B-\frac{2}{R^2\zeta},$$

$$C=-\frac{2\zeta}{R}\frac{\partial R}{\partial\eta}.$$

The boundary and symmetry conditions (5)–(10) are now:

at $\eta=\pm\Lambda/2$,

$$\psi=0, \qquad \omega=\frac{1}{\zeta}\frac{\partial^2\psi}{\partial\eta^2}, \qquad T=0; \tag{22}$$

at $\zeta=0$,

$$\psi=0, \qquad \omega=0, \qquad \partial T/\partial\zeta=0; \tag{23}$$

at $\zeta=1$,

$$\psi=0, \tag{24}$$

$$\omega=\frac{1}{R}\left(\frac{\partial R}{\partial\eta}\right)^2\frac{\partial w}{\partial\zeta}-2\frac{\partial R}{\partial\eta}\frac{\partial w}{\partial\eta}+\left[2-\left(\frac{\partial R}{\partial\eta}\right)^2\right]\frac{\partial u}{\partial\eta}+\frac{1}{R}\left(\frac{\partial R}{\partial\eta}\right)^3\frac{\partial u}{\partial\zeta}+\left[1+\left(\frac{\partial R}{\partial\eta}\right)^2\right]^{1/2}\frac{\partial T}{\partial\eta}, \tag{25}$$

$$\frac{1}{(1+(\partial R/\partial\eta)^2)^{1/2}}\left[\frac{1}{R}\frac{\partial T}{\partial\zeta}-\frac{\partial R}{\partial\eta}\left(\frac{\partial T}{\partial\eta}-\frac{1}{R}\frac{\partial R}{\partial\eta}\frac{\partial T}{\partial\zeta}\right)\right]+B_i(T-T_\infty)=0, \tag{26}$$

$$p-G\eta+\lambda-\frac{2Re^{-1}}{1+((\partial R/\partial\eta)^2}\left[\frac{1}{R}\frac{\partial u}{\partial\zeta}+\left(\frac{\partial R}{\partial\eta}\right)^2\left(\frac{\partial w}{\partial\eta}-\frac{1}{R}\frac{\partial R}{\partial\eta}\frac{\partial w}{\partial\zeta}\right)-\frac{\partial R}{\partial\eta}\left(\frac{1}{R}\frac{\partial w}{\partial\zeta}+\frac{\partial u}{\partial\eta}-\frac{1}{R}\frac{\partial R}{\partial\eta}\frac{\partial u}{\partial\zeta}\right)\right]$$
$$=Re^{-1}(C_0^{-1}-T)\frac{1}{[1+(\partial R/\partial\eta)^2]^{3/2}}\left(\frac{1+(\partial R/\partial\eta)^2}{R}-\frac{\partial^2 R}{\partial\eta^2}\right). \tag{27}$$

Equations (24) and (25) are the kinematic condition for the surface (i.e. the condition that a point on the surface remain on the surface) and the balance of tangential forces respectively. The complete streamfunction, velocity and temperature fields can be determined for a given axisymmetric surface shape (e.g. starting with an initial guess) using only (19)–(26). Then, as long as the balance-of-force condition (27) is not well satisfied, the force balance residual provides a basis for determining an improved estimate of the free surface shape. This procedure continues until the convergence criteria (to be defined later) are satisfied.

3.2. Solution method

Various methods can be devised to obtain a steady solution of equations (19)–(26). For the sake of simplicity a pseudo-unsteady method in association with a semi-implicit time discretization is used.

We first consider the following system of equations:

$$\frac{\partial T}{\partial\tau}+\left(L_1-\frac{1}{Ma}\nabla^2\right)T+S_1=0, \tag{28}$$

$$\frac{\partial\omega}{\partial\tau}+\left(L_2-\frac{1}{Re}\nabla^2\right)\omega+S_2=0, \tag{29}$$

$$\frac{\partial\psi}{\partial\tau}-\nabla^{*2}\psi+S_3=0, \tag{30}$$

where

$$L_1=\frac{1}{R^2\zeta}\left(\frac{\partial\psi}{\partial\eta}\frac{\partial}{\partial\zeta}-\frac{\partial\psi}{\partial\zeta}\frac{\partial}{\partial\eta}\right), \tag{31}$$

$$L_2=\frac{1}{R^2\zeta}\left(\frac{\partial\psi}{\partial\eta}\frac{\partial}{\partial\zeta}-\frac{\partial\psi}{\partial\zeta}\frac{\partial}{\partial\eta}\right)-\frac{u}{R\zeta}, \tag{32}$$

$$\nabla^2=\frac{\partial^2}{\partial\eta^2}+A\frac{\partial^2}{\partial\zeta^2}+B\frac{\partial}{\partial\zeta}, \tag{33}$$

$$\nabla^{*2}=\frac{\partial^2}{\partial\eta^2}+A\frac{\partial^2}{\partial\zeta^2}+B^*\frac{\partial}{\partial\zeta}, \tag{34}$$

$$S_1=-\frac{1}{Ma}C\frac{\partial^2 T}{\partial\eta\partial\zeta},\qquad S_2=\frac{1}{Re}\left(\frac{\omega}{R^2\zeta}-C\frac{\partial^2\omega}{\partial\eta\partial\zeta}\right)+\frac{Gr}{Re^2}\frac{1}{R}\frac{\partial T}{\partial\zeta}, \tag{35}$$

$$S_3=-C\frac{\partial^2\psi}{\partial\eta\partial\zeta}+R\zeta w. \tag{36}$$

We then proceed to solve this system as the (pseudo) time derivatives of T, ψ and $\omega\to 0$. For clarity we present the solution method only for the vorticity (ω) transport equation. The

discretization in time employs an explicit Adams–Bashforth scheme for the non-linear convective terms and the implicit scheme for the viscous terms. Other terms in the equation are treated explicitly. For spatial discretization, central differences are used. The ADI form for the vorticity equation is then

$$\frac{2}{\Delta\tau}\left(\omega_{ij}^{n+1/2}-\omega_{ij}^{n}\right)+\tfrac{3}{2}(L_2\omega)_{ij}^{n}-\tfrac{1}{2}(L_2\omega)_{ij}^{n-1}-\frac{1}{Re}\left(\frac{\partial^2\omega}{\partial\eta^2}\right)_{ij}^{n}-\frac{1}{Re}\left(A\frac{\partial^2\omega}{\partial\zeta^2}+B\frac{\partial\omega}{\partial\zeta}\right)_{ij}^{n+1/2}+(S_2)_{ij}^{n}=0, \tag{37}$$

$$\frac{2}{\Delta\tau}(\omega_{ij}^{n+1}-\omega_{ij}^{n+1/2})+\tfrac{3}{2}(L_2\omega)_{ij}^{n}-\tfrac{1}{2}(L_2\omega)_{ij}^{n-1}-\frac{1}{Re}\left(\frac{\partial^2\omega}{\partial\eta^2}\right)_{ij}^{n+1}-\frac{1}{Re}\left(A\frac{\partial^2\omega}{\partial\zeta^2}+B\frac{\partial\omega}{\partial\zeta}\right)_{ij}^{n+1/2}+(S_2)_{ij}^{n}=0. \tag{38}$$

Here the superscript $n+1/2$ denotes the intermediate step associated with the ADI method.[16] The velocities of (25) (at the nth step) are taken from the values at the previous step. Thus, except for the thermal condition at the free boundary, these are Dirichlet boundary conditions. The heat transfer equation is also discretized in an ADI form. The resulting system of discretized equations is solved using a factorization method.[16]

We define a steady state to occur when the residuals ($\partial\omega/\partial\tau$, $\partial T/\partial\tau$, $\partial\psi/\partial\tau$) of the vorticity, energy and streamfunction equations are less than 10^{-7}, i.e.

$$\max\left|\frac{F_{ij}^{n+1}-F_{ij}^{n}}{\Delta\tau}\right|<10^{-7}. \tag{39}$$

Here F represents the vorticity, temperature or streamfunction, the subscript refers to the spatial location and the superscript refers to the iterative step. The numerical solution is second-order-accurate in space.

We have verified this solution method for steady 2D axisymmetric incompressible flow. Table I shows four examples of a comparison between the results of our code and a finite element code (FIDAP): two for buoyancy- and two for thermocapillary-driven flow. Figure 2 shows a comparison of the surface velocities using our method and the finite element method. One sees that the numerical method described here provides a reasonably accurate algorithm for computing steady 2D axisymmetric incompressible flows in rigid cavities and for mixed buoyancy- and surface-driven flows with free boundaries for the range of surface Reynolds numbers examined, $0<Re<21\,740$.

Having computed the vorticity and streamfunction for a given surface shape, it remains to iterate on the condition for the force balance normal to the surface in order to obtain the final steady surface shape. In addition, the shape must satisfy the volume constraint (11) and boundary conditions (12).

Table I. Comparison of finite difference method with results obtained using finite element code FIDAP

				This method		FIDAP	
Λ	Pr	Ra	Re	W_{max}	U_{max}	W_{max}	U_{max}
2	1	100	0	$1{\cdot}81\times10^{-1}$	$4{\cdot}27\times10^{-2}$	$1{\cdot}80\times10^{-1}$	$4{\cdot}28\times10^{-2}$
2	1	150	0	$2{\cdot}84\times10^{-1}$	$6{\cdot}64\times10^{-2}$	$2{\cdot}66\times10^{-1}$	$6{\cdot}64\times10^{-2}$
2	0·0127	0	3150	3·39	1·7	3·49	1·82
5·2	0·0127	0	5905	2·95	1·33	2·78	1·29

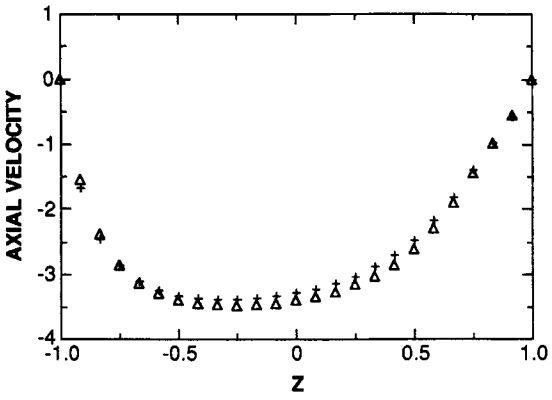

Figure 2. Comparison of surface velocities calculated for $Re=3150$, $Gr=0$ and $Pr=0{\cdot}0127$ using FIDAP and our method ($N_r \times N_z = 25 \times 49$)

Two iterative schemes for determining the surface are discussed in this section. In both schemes the new velocities and temperatures are taken from the current calculated values and the pressure at the surface can be obtained by taking the η-component of the momentum equation and integrating with respect to η. This yields

$$p=\int_0^{\eta}\left[-\frac{1}{R}\left(\frac{\partial\psi}{\partial s}\frac{\partial w}{\partial\zeta}-\frac{\partial\psi}{\partial\zeta}\frac{\partial w}{\partial s}\right)+\frac{1}{Re}\left(\frac{\partial^2 w}{\partial s^2}+A\frac{\partial^2 w}{\partial\zeta^2}+B\frac{\partial w}{\partial\zeta}+C\frac{\partial^2 w}{\partial s\,\partial\zeta}\right)+\frac{Gr}{Re^2}T\right]\left(1+\left(\frac{\partial R}{\partial s}\right)^2\right)^{1/2}\mathrm{d}s. \tag{40}$$

Scheme I is based on the following principle. A shape is assigned to the free surface with the calculated pressure, velocity and temperature. An initial guess for the pressure constant λ is made. The new surface shape is then determined directly from (27)using finite differences in conjunction with Newton's method. The integral (11) is then evaluated to check whether the volume constraint has been satisfied. If it is not satisfied, an inner iteration is made using a Newton–Raphson procedure to calculate the following improved estimate of λ:

$$\lambda^{k+1}=\lambda^k-\left(\frac{\partial V}{\partial\lambda}\right)^{-1}\Delta V, \tag{41}$$

where

$$\Delta V=\int_{-\Lambda/2}^{\Lambda/2}\pi R^2\mathrm{d}\eta-V_0. \tag{42}$$

The above procedure for determining λ is quite effective and is repeated until the volume constraint is satisfied. $R(\eta)$ is then updated. New velocity, pressure and temperature fields are calculated using the updated value of $R(\eta)$. The outer iteration is repeated until

$$ER=\max\left|\frac{R^{m+1}-R^m}{R^m}\right|<\varepsilon, \tag{43}$$

where we took $\varepsilon=10^{-4}$.

Scheme II, after Ryskin and Leal,[15] uses the residual of the force balance condition normal to the surface to drive the shape to its steady position. This is equivalent to equating the residual with an artificial capillary force. This effective force causes a local displacement of the surface in

the direction of the force. The magnitude of the local displacement is proportional to this force. The surface shape at each iteration is thus modified so as to reduce the residual until condition (27) is met. It follows that at each iteration the new position of the surface is given by

$$R_j^{m+1} = R_j^m + \alpha Ex_j, \tag{44}$$

where Ex_j is the residual of the force balance equation at the jth surface location and the constant coefficient α is determined by numerical experiment. In order to ensure convergence, α should be small. If α is chosen to be too small, the convergence is slow and the amount of CPU time used increases substantially. If α is too large, the solution will diverge. We found that the values of α which led to rapid convergence depend on the product of Re^{-1} and C_0^{-1} (see Table II).

The change in volume between the mth and $(m+1)$th iteration can be found from the volume constraint (11) and equation (44) and neglecting higher-order terms, i.e.

$$\int_{-\Lambda/2}^{\Lambda/2} Ex_j R_j^m \mathrm{d}\eta = 0. \tag{45}$$

The pressure constant λ is contained in Ex_j and is obtained by satisfying (45). Even then the liquid bridge may still change the volume slightly at each iteration owing to numerical error and higher-order effects. These small changes can accumulate and eventually result in a gross error. To prevent this, formula (44) is modified to

$$R_j^{m+1} = R_j^m \left(\frac{V_0}{V_m}\right)^{1/2} + \alpha Ex_j. \tag{46}$$

3.3. Convergence behaviour

The rate of convergence of the two methods is shown in Figure 3 for $Re = 695$ and 2082. In both cases the shapes of the curves clearly reflect the procedure used. The curves show two distinct segments. The abrupt rise in the residual in the late stages of the calculation is caused by requiring a more accurate solution (smaller residual) for the vorticity and streamfunction.

For the calculations carried out here, the first outer iteration scheme converged slightly faster than the second. This is shown in Table III. If the guess for the initial iterate is good, the computation times are about equal. For a poor guess, however, the first scheme is 1·5 times faster. While we were able to obtain convergence for all cases attempted using scheme II, this was not the case for scheme I. We found the first scheme to be quite sensitive to the initial choice of the pressure constant λ. If the value of λ is 'physically unreasonable', the solution diverges. In order to take advantage of the speed afforded by scheme I, we employed the second scheme to calculate the value of λ for the first few iterations. This value is then taken as an initial guess for the first scheme, which is used for the remaining outer iterations.

The convergence of the solution was also checked by varying the spatial resolution of the mesh. This was particularly important at higher values of Re where, owing to the space-centred differences, the streamfunction was prone to exhibit 'wiggles' if the grid Peclet number $Pe_{\text{grid}} = U^*\Delta/\kappa$ (where Δ is the interval between two grid points) exceeded 2 in the vicinity of the

Table II. Optimal values of α as a function of $Re^{-1}C_0^{-1}$

$Re^{-1}C_0^{-1}$	20	2	0·2	0·1	0·06
α	10^{-5}	10^{-4}	10^{-3}	2×10^{-3}	$3{\cdot}3\times10^{-3}$

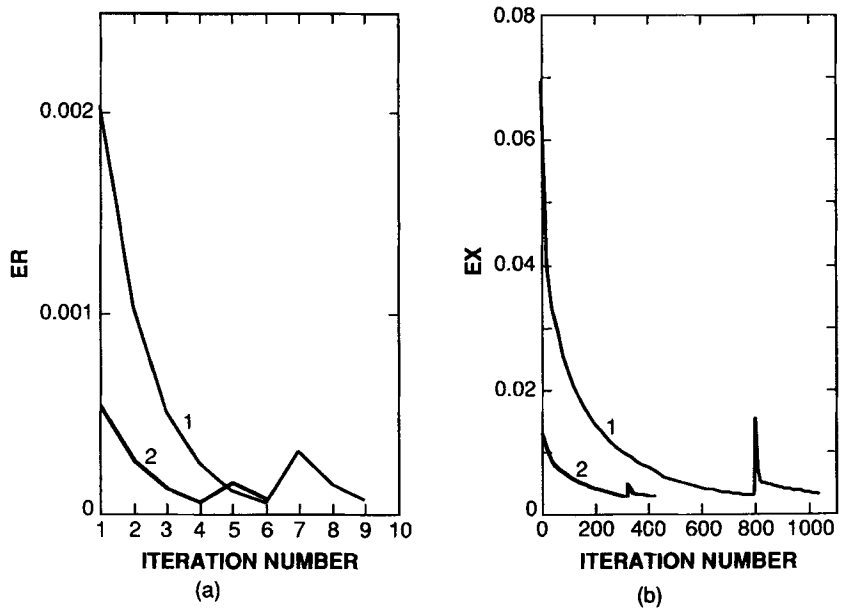

Figure 3. Comparison of convergence rates for (a) scheme I and (b) scheme II

Table III. Sample comparison of CPU times for schemes I and II and for the type of initial guess. The parameters are $\Lambda = 2$, $Pr = 0{\cdot}023$, $Ma = 48$, $Gr = 76$, $C_0 = 4{\cdot}5 \times 10^{-3}$ and $Bi = 100$. A 'good guess' refers to the equilibrium shape of the bridge and a 'poor guess' specifies the surface shape as $R(z) = 1 + 0{\cdot}006 \sin[\pi(z+1)]$.

	Computation time (s)	
Initial guess	Scheme I	Scheme II
Good	70	72
Poor	130	332

disks. The wiggles are present for $N_r \times N_z = 26 \times 61$ and are not eliminated until $N_z = 101$. As observed by Ryskin and Leal,[15] an increase in the mesh resolution was found to eliminate this problem. We attempted to eliminate the wiggles and avoid the need for mesh refinement by employing second- and third-order upwind schemes for convective terms. We found that while the wiggles were certainly eliminated for $N_r \times N_z = 26 \times 61$ (see Figure 4), the mesh still needed to be refined in order to obtain grid convergence. Since the end result was the same, we concluded that the centred difference scheme was preferable. A mesh of $N_r \times N_z = 26 \times 51$ was found to be sufficient for the results presented here with Reynolds numbers in the range $0 < Re < 10\,000$.

We have used the method described earlier to examine the influence of various parameters on momentum and heat transport and meniscus shape. In addition, a favourable comparison for full and half-zones has been made between the results obtained using the combined scheme and those of Hyer *et al.*[11] who employed a finite element scheme.

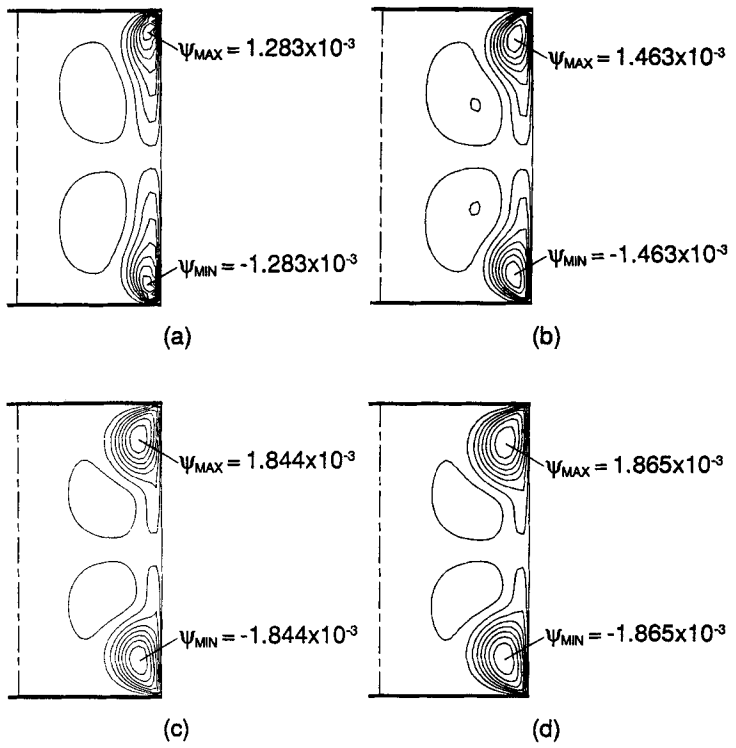

Figure 4. Comparison of results obtained using (a) $N_z = 61$, central finite differences, (b) $N_z = 61$, third-order upwinding, (c) $N_z = 101$, central finite differences and (d) $N_z = 101$, third-order upwinding

The effects of varying the temperature difference ΔT (keeping Gr/Re fixed), the Reynolds number Re, the Biot number Bi, the aspect ratio Λ and the Grashof number Gr are presented in the following section.

4. RESULTS

4.1. Effects of an increase in ΔT at fixed Gr/Re

Figure 5 shows the meniscus shape, dimensionless streamlines and isotherms calculated for a fluid with the properties of $Gd_5Ga_5O_{12}$, $Pr = 4{\cdot}67$, $Bi = 100$, $Re = 21{\cdot}4$, 107, 215 and 1073 ($Ma = 100$, 500, 1002 and 5010) and $Gr/Re = 0{\cdot}025$. In all cases the surface tension decreases with increasing temperature. This creates a force tangent to the surface which drives the melt towards the disks and results in the formation of two toroidal rolls with opposite senses of rotation. The gravitational acceleration results in a surface shape that bulges out below $z = 0$ and necks in above it. This causes an asymmetry in the structure of the two rolls, with the lower roll being more intense.

At $Re = 21{\cdot}4$ ($Ma = 100$) heat transport is governed by conduction. In the centre, heat is transported through and along the surface ($Bi = 100$), which results in a significant component of the temperature gradient perpendicular to the surface. In the vicinity of the disks the transport of heat is mostly through conduction along the surface. At higher values of Re convection is

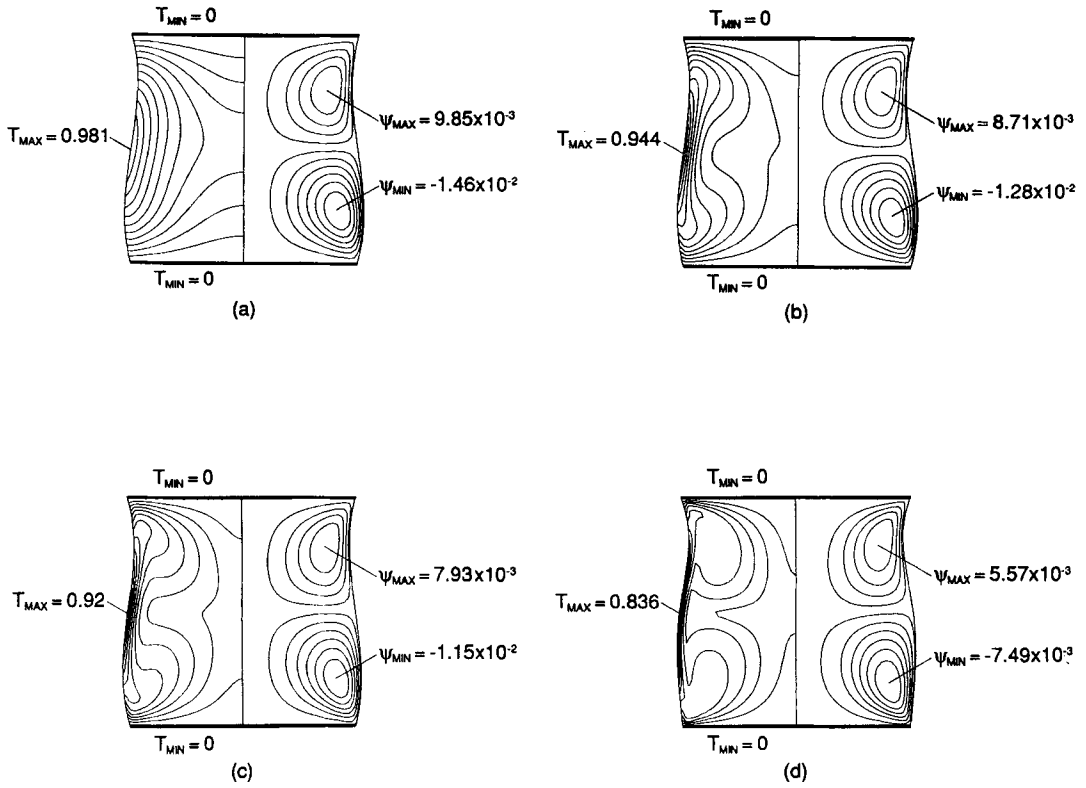

Figure 5. Meniscus shape, streamlines and isotherms calculated for a fluid with the properties of $Gd_5Ga_5O_{12}$, $Pr = 4{\cdot}67$, $Bi = 100$ and $Gr/Re = 0{\cdot}025$: (a) $Re = 21{\cdot}4$, $c_T = 0{\cdot}089$, $c_\psi = 2{\cdot}2 \times 10^{-3}$; (b) $Re = 107$, $c_T = 0{\cdot}086$, $c_\psi = 1{\cdot}9 \times 10^{-3}$; (c) $Re = 214{\cdot}6$, $c_T = 0{\cdot}084$, $c_\psi = 1{\cdot}8 \times 10^{-3}$; (d) $Re = 1073$, $c_T = 0{\cdot}084$, $c_\psi = 1{\cdot}2 \times 10^{-3}$. The temperature and streamfunction contour intervals are c_T and c_ψ respectively

intensified. The flow velocities reach their maximum values at locations intermediate between the central portion of the surface and the disks. In the central region of the melt the outward flow towards the surface brings cooler melt from the interior and causes a steep temperature gradient perpendicular to the surface. Towards the end walls the frequency with which isotherms intersect the surface increases. This indicates a steeper temperature gradient parallel to the surface.

Figure 6 shows the effect of increasing Gr and Re at fixed Gr/Re ($= 0{\cdot}036$) for a fluid with the properties of molten silicon. As ΔT is increased, the increase in buoyancy-driven flow in the upper region results in a larger upper cell which extends into the lower half. Note that the ratio of the magnitudes of ψ_{max} to ψ_{min} increases as Gr and Re are increased. It is interesting that, even though Gr/Re is small, if the ratio remains constant but the magnitudes of Gr and Re are increased, the buoyancy-driven effect manifests itself more at higher Gr- and Re-values. There is an increase in buoyancy effect due to the (vertically) thermally unstable situation in the upper half which acts together with the radial temperature gradients throughout the liquid bridge to produce a downward motion of colder fluid in the region midway between the axis and the surface. As a result, buoyancy-driven flow becomes pervasive throughout the system and confines the more intense (thermocapillary-driven) cell to a small region in the lower half.

The effect of increasing ΔT on the free surface shape is insignificant for these cases.

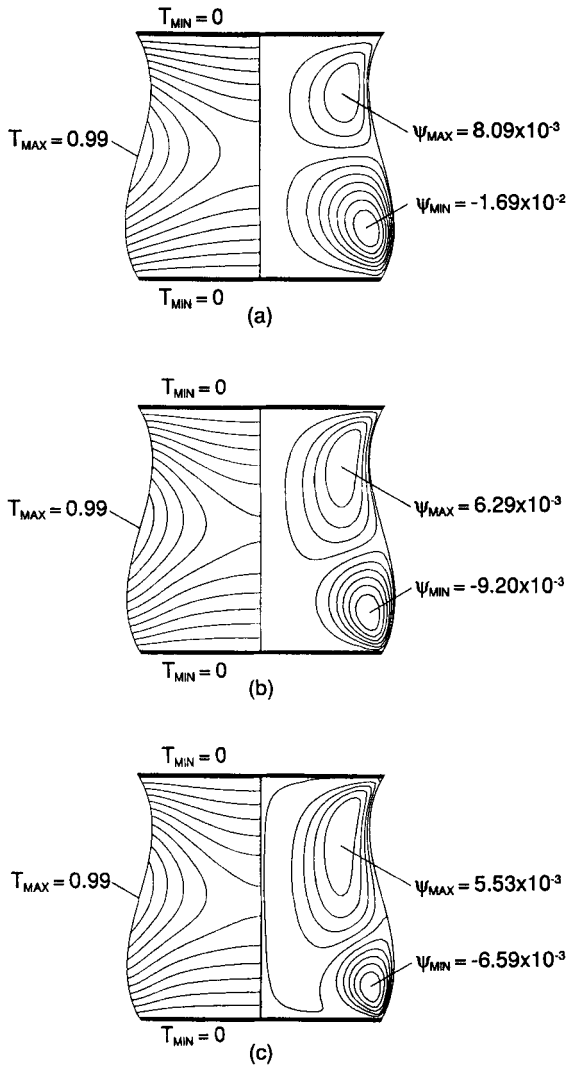

Figure 6. Meniscus shape, streamlines and isotherms calculated for a fluid with the properties of molten silicon, $Pr = 0{\cdot}023$, $Bi = 100$ and $Gr/Re = 0{\cdot}036$: (a) $Re = 139$, $c_\psi = 2{\cdot}3 \times 10^{-3}$; (b) $Re = 1390$, $c_\psi = 1{\cdot}4 \times 10^{-3}$; (c) $Re = 2082$, $c_\psi = 1{\cdot}1 \times 10^{-3}$; $c_T = 0{\cdot}09$ for all three cases

4.2. Effect of Biot number

The effect of Bi on the liquid bridge shape is slight for the cases examined. The isotherm distribution is modified, however, when Bi is increased from 10 to 100 (see Figures 5(b) and 7). In the central part of the surface the temperature gradient is almost perpendicular to the surface in both cases. For $Bi = 100$ the gradient is steeper and the temperature in the central region is higher, which results in a steeper temperature gradient parallel to the surface near the disks. There is a slight decrease in flow intensify for the $Bi = 10$ case.

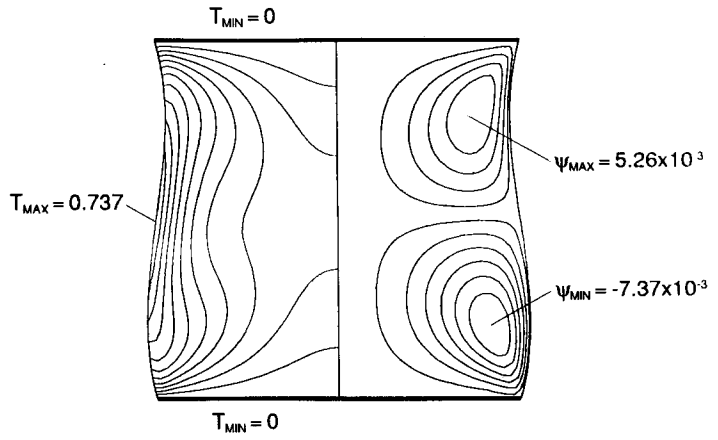

Figure 7. Effect of Bi (compare with Figure 5) for $Bi = 10$, $Pr = 4{\cdot}667$, $Re = 107$, $C_0^{-1} = 70$, $G = 0{\cdot}468$ and $Gr = 2{\cdot}7$. The streamfunction and temperature contour intervals are $1{\cdot}9 \times 10^{-3}$ and 0·086 respectively

4.3. Effect of aspect ratio (Λ)

For otherwise identical physical conditions a change in aspect ratio of the liquid bridge has a significant effect on the meniscus shape. This is illustrated in Figure 8 by a comparison of liquid bridges with $\Lambda = 2{\cdot}5$ and 3. The shapes are qualitatively similar but the amplitude of the deformation from a right circular cylinder is much larger for the higher aspect ratio. For the large-aspect-ratio bridge there is a relative decrease in flow intensity in the upper part as the flow conforms to the increased curvature of the surface of the longer liquid bridge. The flow intensity of the lower cell is greater for the longer aspect ratios and the isotherms exhibit correspondingly more distortion. Results obtained for $\Lambda = 3{\cdot}2$ confirm this trend (note that with a Bond number $Bo = \rho g R^2/\gamma_0 = 0{\cdot}7$ the $\Lambda = 3{\cdot}2$ bridge is close to the stability limit[17]).

4.4. Pure thermocapillary flow

In the absence of gravity $Gr = B_0 = 0$ and the flow is driven only by surface tension gradients. Figure 9 shows the isotherms and streamlines computed for a fluid with the properties of molten silicon for values of Re up to 21 740. We computed cases with $Re = 1390$, 4350, 8695 and 21 740. At $Re \geqslant 4350$ we found secondary cells. There is an increase in secondary flow intensiy at higher values of Re (see Figures 9(b) and 9(c)). Even at the higher values of Re the isotherms are only slightly distorted.

For the finite gravity case ($Gr = 76$) the effects of surface shape and buoyancy-driven flow are manifested (see Figure 10). Only two cells are evident in the finite gravity case. The larger cell appears to be a combination of a primary thermocapillary cell and a downward flow due to buoyancy near the axis, which extends into the central region of the lower half and interacts with a secondary flow cells associated with the thermocapillary flow. The primary thermocapillary-driven cell in the lower half is considerably smaller in extent than it is for the zero-gravity case. A comparison between zero-gravity and finite gravity conditions illustrates the interaction between the weaker buoyancy-driven flow, the secondary thermocapillary cells (see Figures 9 and 10) and the surface shape.

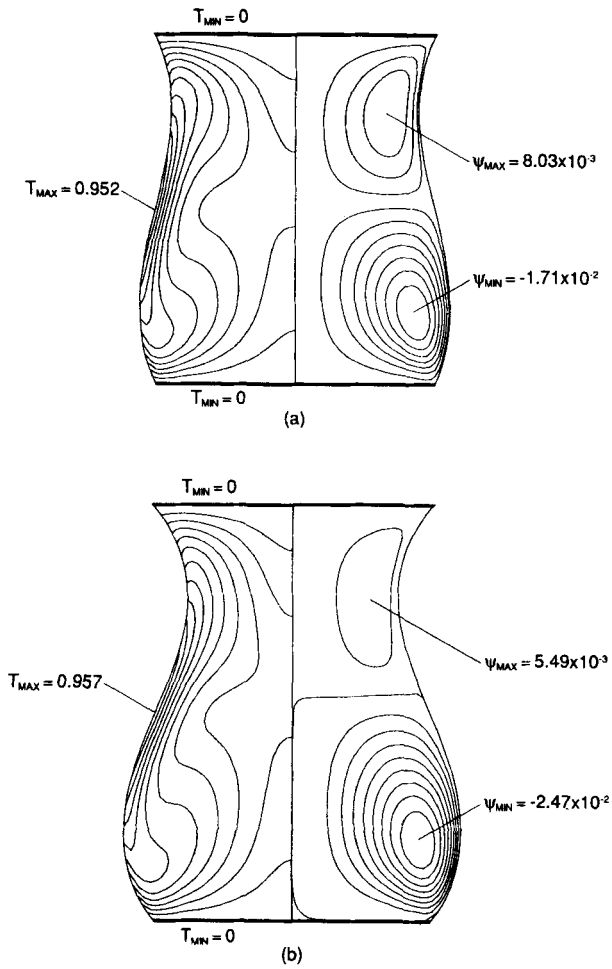

Figure 8. Effect of aspect ratio: (a) $\Lambda = 2{\cdot}5$; (b) $\Lambda = 3$; $Bi = 100$, $B_0 = 0{\cdot}7$, $Pr = 4{\cdot}667$, $Re = 107$, $C_0^{-1} = 70$, $G = 0{\cdot}468$, $Gr = 2{\cdot}7$. The streamfunction contour intervals are $1{\cdot}2 \times 10^{-3}$ and $2{\cdot}3 \times 10^{-3}$ for (a) and (b) respectively and the temperature contour interval is 0·087 for both cases

5. CONCLUSIONS

Steady solutions to the free boundary problem for a non-isothermal liquid bridge have been obtained using a Picard-type iterative scheme with a semi-implicit space-centred finite difference scheme. The method was applied to a variety of problems with Reynolds numbers in the range $0 < Re < 22000$ and for Pradtl numbers of 0·023 and 4·67. The method was found to perform well for this range of parameters examined and compared well with results obtained for buoyancy-driven and surface-tension-driven flow using a finite element method. At high Re we found that the solution was sensitive to the spatial resolution and that a larger number of grid points were necessary in order to avoid 'wiggles' in the solution. For $Re < 10000$ we found $N_r \times N_z = 26 \times 51$ points to be sufficient, but required up to 101 points in the z-direction for $Re = 21\,740$. While it was possible to remove the wiggles using upwind differences, the mesh refinement was still

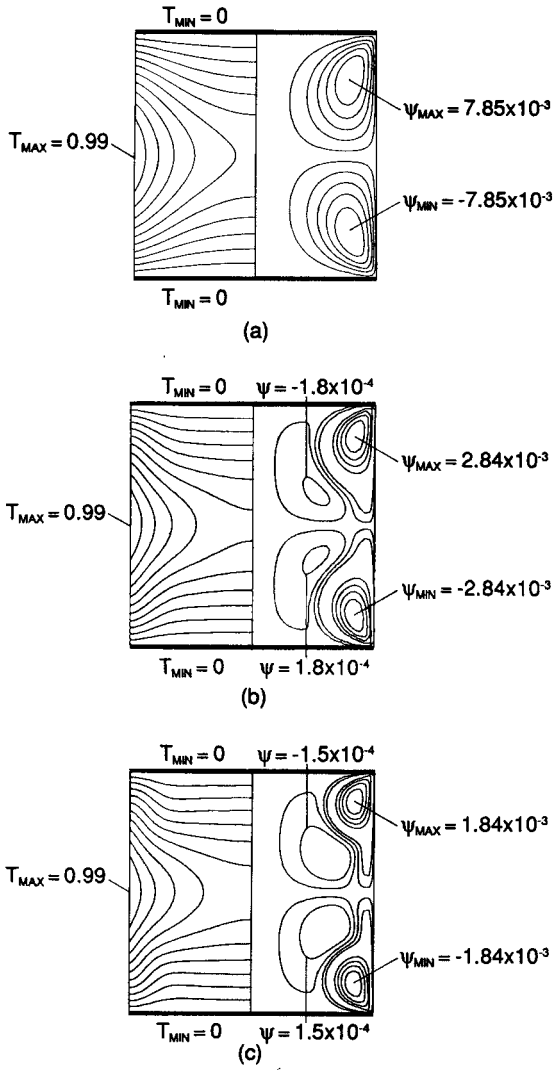

Figure 9. Meniscus shape, streamlines and isotherms calculated for a fluid with the properties of molten silicon, $Pr = 0{\cdot}023$, $Bi = 100$, $Gr = 0$ and $Re =$ (a) 1390, (b) 8695 and (c) 21740. The streamfunction contour intervals are $7{\cdot}7 \times 10^{-4}$, $3{\cdot}7 \times 10^{-4}$ and $2{\cdot}5 \times 10^{-4}$ for (a), (b) and (c) respectively and the temperature contour interval is 0·087 for all three cases

necessary in order to obtain grid convergence. Thus no advantage was obtained by using upwind differencing.

While the parametric study is by no means exhaustive, the results indicate some interesting trends. Perhaps the most interesting behaviour is the response to an increase in the effective maximum temperature difference ΔT. It was found that for a non-zero Grashof number an increase in ΔT caused an increase in intensity of the cell in the lower half of the bridge. For the low-Prandtl-number case it was found that at higher values of ΔT the spatial extent of the lower cell actualy decreased as the less intense upper cell penetrated into the lower part. This can be explained by the increasing importance of radial temperature gradients in driving buoyant flow as

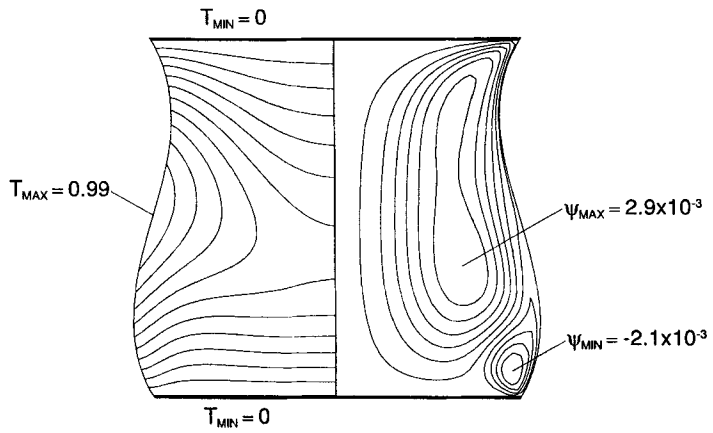

Figure 10. Meniscus shape, streamlines and isotherms calculated for a fluid with the properties of molten silicon, $Pr = 0{\cdot}023$, $Bi = 100$, $Gr = 76$ and $Re = 8695$. The streamfunction contour interval is $4{\cdot}6 \times 10^{-4}$ and the temperature contour interval is 0·087

ΔT is increased. As expected from the results of previous work, the effect of changing the aspect ratio was also seen to significantly affect the flow behaviour. For non-zero gravity the increase in convexity of the lower portion of the larger-aspect-ratio bridge has a pronounced effect on the flow pattern, which is more intense for the longer liquid bridge. This increase in flow intensity appears to occur as a result of a decrease in the form drag of the surface. A comparison between the difference in flow intensity between the upper and lower halves reveals that the difference increases with increasing Λ. The form drag in the upper half increases as the magnitude of the negative curvature increases. This slows the flow in the upper half relative to the lower half of the bridge.

ACKNOWLEDGEMENTS

This work was supported by the National Aeronautics and Space Administration through grant NAG8-724 and also by the State of Alabama through the Center for Microgravity and Materials Research and the Alabama Supercomputer Network.

REFERENCES

1. C. Chang and W. R. Wilcox, 'Inhomogeneities due to thermocapillary flow in floating zone melting', *J. Cryst. Growth*, **28**, 8–12 (1975).
2. P. A. Clark and W. R. Wilcox, 'Influence of gravity on thermocapillary convection in floating zone melting of silicon', *J. Cryst. Growth*, **50**, 461–469 (1980).
3. N. Kobayashi, 'Computer simulation of the steady flow in a cylindrical float zone under low gravity', *J. Cryst. Growth*, **66**, 63–72 (1984).
4. W. W. Fowlis and G. O. Roberts, 'Confinement of thermocapillary floating zone flow', *J. Cryst. Growth*, **74**, 301–320 (1986).
5. A. Rybicki and J. M. Floryan, 'Thermocapillary effects in liquid bridges', *Phys. Fluids*, **30**, 1956–1972 (1987).
6. R. Natarajan, 'Thermocapillary flows in a rotating float zone under microgravity', *AIChE J.*, **35**, 614–624 (1989).
7. Z. Kozhoukharova and S. Slavchev, 'Computer simulation of thermocapillary convection in a non-cylindrical floating zone', *J. Cryst. Growth*, **74**, 236–246 (1986).
8. W. G. Pfann, *Zone melting*, Krueger, Huntington, NY, 1978.
9. J. L. Duranceau and R. A. Brown, 'Finite element analysis of melt convection and interface morphology in earthbound and microgravity floating zones', in T. G. Wang (ed.), *Drops and Bubbles Third Int. Colloq. 1988, AIP Conf. Proc., Vol. 197*, American Institute of Physics, New York, 1989, pp. 133–144.

10. C. W. Lan and S. Kou, 'Thermocapillary flow and melt/solid interfaces in floating-zone crystal growth under microgravity', *J. Cryst. Growth*, **102,** 609–627 (1990).
11. J. Hyer, D. F. Jankowski and G. P. Neitzel, 'Thermocapillary convection in a model float zone', *AIAA J. Thermophys. Heat Transfer*, in the press (1991).
12. J. M. Floryan, 'Numerical methods for viscous flows with moving boundaries', *Appl. Mech. Rev.*, **42,** 323–341 (1989).
13. I. S. Kang and L. G. Leal, 'Numerical solution of axisymmetric, unsteady free-boundary problems at finite Reynolds number. I Finite difference scheme and its application to the deformation of a bubble in a uniaxial straining flow', *Phys. Fluids*, **30,** 1929–1940 (1987).
14. H. M. Ettouney and R. A. Brown, 'Finite element methods for steady solidification problems', *J. Comput. Phys.*, **49,** 118–150 (1983).
15. G. Ryskin and L. G. Leal, 'Numerical solution of free boundary problems in fluid mechanics. Part 1. The finite-difference technique', *J. Fluid Mech.*, **148,** 1–17 (1984).
16. R. Peyret and T. D. Taylor, *Computational Methods for Fluid Flow*, Springer, New York, 1983.
17. I. Martinez, J. M. Haynes and D. Langbein, 'Fluid statics and capillarity', in H. U. Walter (ed.), *Fluid Sciences and Materials Science in Space*, Springer, Berlin, 1987, pp. 53–81.